NJC

ROYAL SOCIETY OF CHEMISTRY

PAPER

View Article Online
View Journal | View Issue

Check for updates

Cite this: *New J. Chem.*, 2025, **49**, 109

Structural characterization and tuning of magnetic properties of $CoV_{\delta}Fe_{2-\delta}O_4$ ($0.0 \leq \delta \leq 0.9$) nanomaterials synthesized *via* a modified sol–gel autocombustion method

Anagha B. Patil and Rabi N. Panda *

We report magnetic properties of $CoV_{\delta}Fe_{2-\delta}O_4$ nanomaterials synthesized *via* a modified sol–gel autocombustion method. Lattice parameters obtained from X-ray diffraction (XRD) studies varied from 8.348 to 8.285 Å for δ = 0.0–0.9. Crystallite sizes estimated using Williamson–Hall (W–H) plots were found to be in the range of 52–30 nm (δ = 0.0–0.9). Lattice strain varied from 1.34×10^{-3} to 2.00×10^{-3} for δ = 0.0–0.9. Fourier transform infrared (FTIR) studies revealed peak positions in the ranges of 589.2–602.9 and 409.3–419.5 cm^{-1} for tetrahedral (T_d) and octahedral (O_h) coordination, respectively. Raman spectra showed peaks corresponding to $T_{2g}(3)$, $E_g(2)$, $E_g(1)$, $T_{2g}(2)$, $T_{2g}(1)$, $A_{1g}(2)$ and $A_{1g}(1)$ modes. Particle sizes obtained from field emission scanning electron microscopy (FESEM) analysis varied from 56 to 34 nm for δ = 0.0–0.9. Values of saturation magnetization (M_s) showed significant variation from 82.5 to 47.3 emu g^{-1} for δ = 0.0–0.9. Coercivity (H_c) values (at 300 K) decreased from 1180 (δ = 0.0) to 886 Oe (δ = 0.9). The estimated values of M_s and H_c (at 5 K) varied from 74.8 to 48.9 emu g^{-1} (δ = 0.0 to 0.9) and from 7772 to 7078 Oe (δ = 0.0 to 0.9), respectively. XPS study confirmed the redistribution of Co^{2+} and Fe^{3+} ions in Oh and Td sites, agreeing well with the magnetic behaviour. The observed decrease in H_c values were also related to a decrease in anisotropy constant (K_1), *i.e.* from 1.44×10^4 to 1.19×10^4 J m^{-3} for δ = 0.0–0.9.

Received 8th August 2024,
Accepted 16th November 2024

DOI: 10.1039/d4nj03546a

rsc.li/njc

Open Access Article. Published on 18 November 2024. Downloaded on 5/8/2026 8:39:22 PM.
This article is licensed under a Creative Commons Attribution 3.0 Unported Licence.

1. Introduction

Over the past few decades, spinel ferrites have gained significant attention owing to their numerous potential technological applications, such as targeted drug delivery, biomedical applications, spintronic devices, wastewater treatment, gas-sensing devices, and microwave devices.[1–4] Among the various properties of spinel ferrites, magnetic properties have been well researched and reported by material scientists. Alterations of intrinsic magnetic characteristics, such as coercivity (H_c) and saturation magnetization (M_s), of ferrite materials are significant. However, to achieve desired changes in the magnetic parameters of ferrites, it is important to control their particle size, morphology, surface properties, *etc.* This can be achieved by developing novel synthesis methods to obtain certain set of properties that may help in various application designs. In this regard, the development of newer synthesis routes for substitution of aliovalent dopants in ABO_3 oxide materials in order to obtain enhanced optical and magnetic properties is significant.[5–7] The effect of substituent elements in spinel ferrites has also been widely studied by materials scientists over the past few decades for the above stated purposes.[8–10] One of the most studied and prominent ferrite materials is cobalt ferrite ($CoFe_2O_4$).[11–13] Magnetic and electrical properties shown by $CoFe_2O_4$ make it a suitable candidate for technological applications.[14,15] Excellent properties shown by $CoFe_2O_4$ materials at their bulk level include high H_c (230 Oe at 298 K), high M_s (80 emu g^{-1}) and moderate anisotropy constant (2.65×10^6 to 5.1×10^6 erg cm^{-3}).[16–18] At the nano-scale level, the above-mentioned properties can be altered substantially, which can be attributed to the manifestation of surface effects having the canted spin structure. For example, a large coercivity value (H_c) of 4.3 kOe at room temperature was observed for $CoFe_2O_4$ with a particle size of 30 nm.[19]

Several synthesis methods have been used for the synthesis of un-substituted and substituted cobalt ferrite materials. Among the various synthesis methods, micro-emulsion, co-precipitation, green synthesis, and hydrothermal methods are noteworthy.[20,21] Also, a recently reported vanadium-doped cobalt ferrite material synthesized *via* a solid-state method at 1100 °C showed interesting potential for high-frequency applications.[22] Cobalt ferrite materials synthesized *via* green synthesis methods were reported that would be suitable for

Department of Chemistry, Birla Institute of Technology and Science, Pilani, Goa Campus, Zuarinagar, 403726, Goa, India. E-mail: rnp@goa.bits-pilani.ac.in

Open Access Article. Published on 18 November 2024. Downloaded on 5/8/2026 8:39:22 PM. This article is licensed under a Creative Commons Attribution 3.0 Unported Licence.

therapeutic applications, such as drug carrier and delivery agents.[20] In the crystal structure of spinel ferrites of the type AB_2O_4, the metal cations occupy the tetrahedral and octahedral positions, *i.e.* A and B sites, respectively.[23] Various properties of cobalt ferrite (*e.g.* magnetic properties) can be influenced by numerous factors, such as the synthesis method, annealing temperature, different substituent elements in the crystal lattice, and particle size and shape.[15] Therefore, the substitution of different elements in $CoFe_2O_4$ (either at Fe^{3+} sites or Co^{2+} sites) is an appropriate approach to modify the magnetic properties for application purposes.[15,24,25]

Substituting non-magnetic d-block transition elements (*e.g.* vanadium) in the $CoFe_2O_4$ crystal lattice has attracted much attention because they can induce changes in the values of M_s and H_c, which are of technological importance. Some of the technological applications include magnetic recording, magnetic resonance imaging, and magnetic hyperthermia.[18] Alteration of the magnetic properties as a result of substitution of V^{5+} ion in $CoFe_2O_4$ has been well studied.[22,26,27] The effect of vanadium substitution in cobalt ferrite $CoV_xFe_{2-x}O_4$ ($0.0 \leq x \leq 0.9$) on the magnetic properties of pure $CoFe_2O_4$ has already been studied from different perspectives, including using a modified synthesis strategy, a smaller particle size ranging between 30–8 nm, and cation redistribution in materials.[22,26,27]

Reports on synthesizing phase-pure $CoV_\delta Fe_{2-\delta}O_4$ materials having a higher vanadium content, δ (*i.e.* $0.25 \leq \delta \leq 0.9$), at relatively lower temperature (700 °C) are rare. Substituting various vanadium ions in $CoV_\delta Fe_{2-\delta}O_4$ can change the magnetic properties substantially by inducing cation distribution. Further, it may further reduce the crystallite size and induce lattice strain. These deformations can lead to the generation of larger H_c values in the materials. In addition, low-temperature magnetic studies on vanadium-substituted cobalt ferrite have rarely been reported, if even at all. Therefore, studies on the variation of M_s and H_c in $CoV_\delta Fe_{2-\delta}O_4$ materials performed in a systematic way are merited. Therefore, in this paper, we report the synthesis of pure-phase $CoV_\delta Fe_{2-\delta}O_4$ nanomaterials ($0.0 \leq \delta \leq 0.9$) at 700 °C using a modified sol–gel autocombustion method. The effect of vanadium insertion in $CoV_\delta Fe_{2-\delta}O_4$ nanomaterials was studied specifically with regards to structural modifications of the spinel lattice. We have attempted exhaustive spectroscopic and electron microscopic investigations for materials characterizations. Finally, a correlation of structure of materials is done with the observed room temperature (300 K) and low temperature (5 K) magnetic properties.

2. Experimental

2.1 Synthesis of $CoV_\delta Fe_{2-\delta}O_4$ ($0.0 \leq \delta \leq 0.9$) nanomaterials

Synthesis of the $CoV_\delta Fe_{2-\delta}O_4$ nanomaterials (δ = 0.0, 0.1, 0.3, 0.5, 0.7, and 0.9) was carried out using a modified citric acid-assisted sol–gel autocombustion method.[26] To be noted, the synthesis procedure adopted in this study has some similarities with the Pechini sol–gel process.[5,6] In summary, Fe $(NO_3)_3 \cdot 9H_2O$ (99%, Molychem, India) and $CoCl_2 \cdot 6H_2O$ (99%, Molychem, India) were taken in desired stoichiometric ratios and dissolved in a minimum quantity of distilled water in separate beakers. V_2O_5 (99% Fisher Scientific, India) was dissolved in water using 1 M NaOH solution, followed by maintaining an acidic pH of 1.5 using 1 M HNO_3. These solutions containing V^{5+}, Co^{2+}, and Fe^{3+} ions were mixed together quantitatively, then transferred to a round-bottom (RB) flask and diluted to 400 mL using distilled water. Citric acid (10.0 g) was added at this stage and the reaction mixture was stirred for 10 min. By the addition of 1 M aq. HNO_3, the pH of the solution mixture was maintained at 1.33. The final solution was then refluxed at 80 °C for 3 h. Next, a viscous gel was formed at 90 °C by the simple process of evaporation using a hot plate. The resulting gel was transformed into a swollen gel when heat treated at 90 °C in a hot air oven for a duration of 6 h. The resulting swollen gel was then crushed and combusted at 400 °C in a muffle furnace (air atmosphere) for a period of 3 h. The resulting black-coloured powdered product was then digested using distilled water (approximately 100 mL) for nearly 10 min, and then the suspension was filtered and washed with distilled water several times. This final pure vanadium-substituted cobalt ferrite product was subjected to annealing at 700 °C for 3 h in a muffle furnace in an air atmosphere, and the final product was used for the subsequent characterization.

2.2 Characterization techniques

$CoV_\delta Fe_{2-\delta}O_4$ ($0.0 \leq \delta \leq 0.9$) nanomaterials, annealed at 700 °C, were characterized using the powder X-ray diffraction (XRD) technique (Bruker, D8 Advance X-ray diffractometer), field emission scanning electron microscopy (FESEM) with energy dispersive spectroscopy (EDS) (QUANTA, FEG 250), Fourier transform infrared spectroscopy (FTIR) (Shimadzu, IRAffinity-1S), Raman spectroscopy (LAB RAM HR Horiba France), and X-ray photoelectron spectroscopy (XPS) (Thermo-Fisher Scientific). The XPS instrument was equipped with a monochromatic Al K_α X-ray source ($h\nu$ = 1486.6 eV). The samples were sputtered with an Ar^+ ion gun for 1 min using 500 eV energy before recording the XPS spectra. The XRD patterns were recorded using CuKα radiation with a 3° min^{-1} scan rate. The crystallite sizes were calculated using Scherrer's formula ($D = (0.9\lambda)/(\beta \cos\theta)$), where D is the average crystallite size, λ is the wavelength of the X-rays, β is the full width at half maximum expressed in radian (FWHM), and θ is the diffraction angle in radian.[28] Also, Williamson–Hall (WH) plots (*i.e.* $\beta\cos(\theta)$ *vs.* $4\sin(\theta)$) were used to determine the lattice strain and crystallite size of the materials. In particular, the WH plots were linearly fitted in order to obtain the slope and Y-intercept values, from which the lattice strain (ε) and crystallite sizes were estimated for the $CoV_\delta Fe_{2-\delta}O_4$ lattice, respectively. To be noted, the Williamson–Hall plot is based on the expression, $[(\beta\cos\theta) = (0.9\lambda/D) + (\varepsilon 4\sin\theta)]$, where ε represents the lattice strain, θ is the diffraction angle, β is full width at half maximum (FWHM) expressed in radian, D is the crystallite size, and λ is the wavelength of X-ray radiation.[29] The FESEM images were analysed for obtaining the morphology and particle sizes of the

 This journal is © The Royal Society of Chemistry and the Centre National de la Recherche Scientifique 2025

Open Access Article. Published on 18 November 2024. Downloaded on 5/8/2026 8:39:22 PM.
This article is licensed under a Creative Commons Attribution 3.0 Unported Licence.

$CoV_\delta Fe_{2-\delta}O_4$ nanomaterials under study. The average particle sizes were estimated using ImageJ software with the maximum number of particles distributed throughout the FESEM image. EDS was carried out for confirming the presence of V, Fe, Co, and O in $CoV_\delta Fe_{2-\delta}O_4$ materials. The elemental compositions were also investigated through the EDS spectra and were in good agreement with the stoichiometry of the materials. For the FTIR studies, the samples were ground with solid KBr powder (in an approximately 1 : 20 ratio) and formed into transparent discs. The powdered $CoV_\delta Fe_{2-\delta}O_4$ samples were used directly for the Raman spectroscopic measurements. For the magnetic properties studies, vibrating sample magnetometry (VSM) was used (Quantum Design, PPMS Evercool II) and the measurements were carried out at room temperature (300 K) and at low temperature (5 K) using a maximum field strength of 2T.

3. Results and discussion

3.1 X-Ray diffraction studies

In Fig. 1, the XRD patterns for the $CoV_\delta Fe_{2-\delta}O_4$ nanomaterials annealed at 700 °C are depicted. Analysis of the XRD patterns for the $CoV_\delta Fe_{2-\delta}O_4$ materials confirmed the single-phase product formation with an inverse cubic spinel ferrite crystal structure. The XRD lines were indexed to ICDD card no. 00-003-0864. The peak indexing for the XRD patterns included reflections from the (220), (311), (222), (400), (422), (511), and (440) planes. For pure $CoFe_2O_4$ materials annealed at 700 °C, reflections from the (220), (311), (222), (400), (422), (511), and (440) planes occurred at 2θ values of 30.25°, 35.70°, 37.34°, 43.31°, 53.74°, 57.29°, and 62.91°, respectively. As the V content increased in $CoV_\delta Fe_{2-\delta}O_4$, there was a shift in the XRD line positions. The XRD lines coinciding to the (311) plane as a function of increasing vanadium content, δ, for $CoV_\delta Fe_{2-\delta}O_4$ ($0.0 \leq \delta \leq 0.9$) are shown in Fig. 2. As the vanadium content (δ) increased in the lattice, there was a shift of the (311) diffraction line initially towards lower values of 2θ up to $\delta = 0.3$, after which it shifted towards higher values of 2θ. In particular, for vanadium contents δ = 0.0, 0.1, 0.3, 0.5, 0.7, and 0.9, the corresponding peak positions (2θ) for the (311) lines were found at 35.70°, 35.61°, 35.64°, 35.80°, 35.72°, and 35.97°, respectively. The shift in the values of 2θ towards lower angles for δ = 0.0, 0.1 and 0.3 concurred with the corresponding values of the lattice parameters showing the lattice expansion, as can be noted in Table 1. Then, for the materials with a higher V content (*i.e.* δ = 0.5, 0.7 and 0.9), the shift in the values of 2θ were observed towards higher values of 2θ, with the lattice parameters showing a systematic decrease for δ = 0.5, 0.7, and 0.9 in $CoV_\delta Fe_{2-\delta}O_4$ (Table 1).

The variation in crystallite sizes and lattice parameters with increasing vanadium content 'δ' ($CoV_\delta Fe_{2-\delta}O_4$, $0.0 \leq \delta \leq 0.9$) is depicted in Fig. 3. It could be observed that there was an overall decrease in the crystallite sizes and lattice parameters as

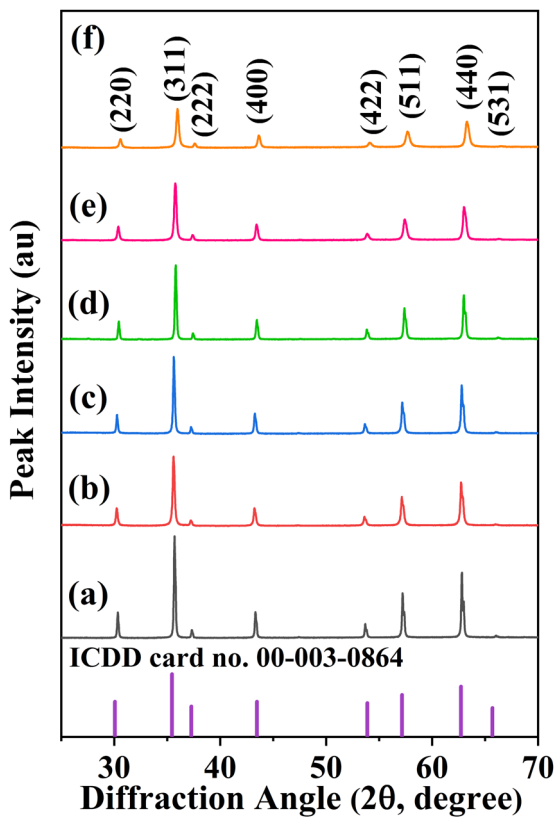

Fig. 1 XRD patterns of $CoV_\delta Fe_{2-\delta}O_4$ ($0.0 \leq \delta \leq 0.9$) nanomaterials annealed at 700 °C (air atmosphere) for different vanadium contents, δ: (a) 0.0, (b) 0.1, (c) 0.3, (d) 0.5, (e) 0.7 and (f) 0.9 together with the XRD pattern for ICDD card no. 00-003-0864.

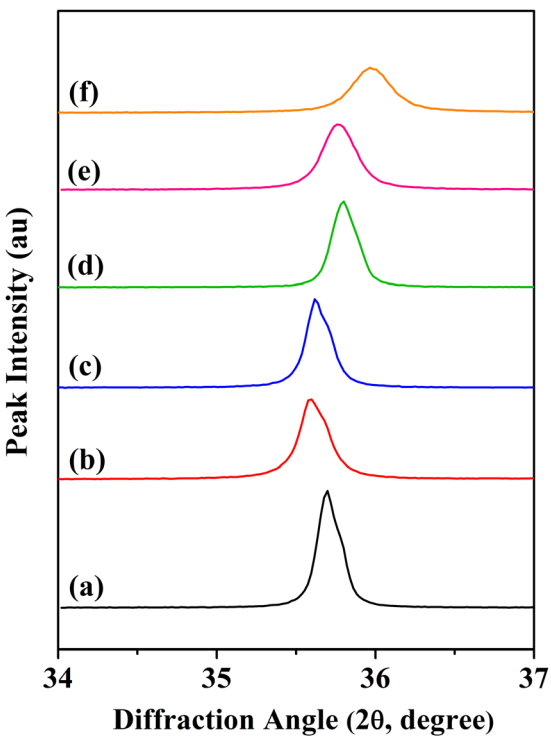

Fig. 2 Shift in the (311) line for $CoV_\delta Fe_{2-\delta}O_4$ ($0.0 \leq \delta \leq 0.9$) nanomaterials annealed at 700 °C for different vanadium contents, δ: (a) 0.0, (b) 0.1, (c) 0.3, (d) 0.5, (e) 0.7 and (f) 0.9.

Open Access Article. Published on 18 November 2024. Downloaded on 5/8/2026 8:39:22 PM.
This article is licensed under a Creative Commons Attribution 3.0 Unported Licence.

Table 1 Material compositions, lattice parameters, lattice volume, crystallite sizes, lattice strain, and FESEM particle sizes of $CoV_\delta Fe_{2-\delta}O_4$ ($0.0 \leq \delta \leq 0.9$) nanomaterials annealed at 700 °C

Material composition $CoV_\delta Fe_{2-\delta}O_4$	Lattice parameters, a (Å)	Volume of unit cell, a^3 (Å^3)	Crystallite size from Scherrer's formula (nm)	Crystallite size from WH plot (nm)	Lattice strain by WH plot ($\times 10^{-3}$)	FESEM particle size (nm)
$\delta = 0.0$	8.348	581.76	43	52	1.34	56
$\delta = 0.1$	8.365	585.33	34	39	1.44	37
$\delta = 0.3$	8.361	584.49	40	49	1.77	48
$\delta = 0.5$	8.326	577.18	40	48	1.57	41
$\delta = 0.7$	8.324	576.76	31	38	2.01	37
$\delta = 0.9$	8.285	568.69	25	30	2.00	34

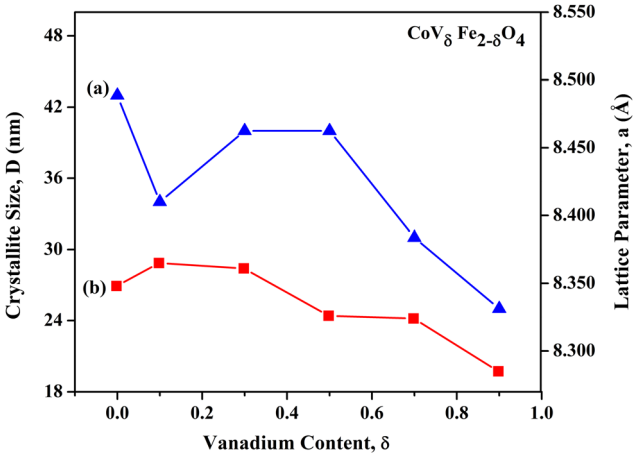

Fig. 3 Variation in (a) crystallite sizes, D, and (b) lattice parameters, a, with increasing V content 'δ' in $CoV_\delta Fe_{2-\delta}O_4$ ($0.0 \leq \delta \leq 0.9$) nanomaterials annealed at 700 °C in an air atmosphere.

the V content increased from $\delta = 0.0$ to $\delta = 0.9$ in $CoV_\delta Fe_{2-\delta}O_4$. A significant decrease in crystallite size from 43 nm for $\delta = 0.0$ to 34 nm for $\delta = 0.1$ was observed. Thereafter, it increased, showing a broad hump centred at $\delta = 0.3$. Then, a drastic decrease in the crystallite sizes was observed, *i.e.* from 40 nm to 25 nm for $\delta = 0.5$ to $\delta = 0.9$, respectively, for the $CoV_\delta Fe_{2-\delta}O_4$ nanomaterials. An overall decrease in the lattice parameters was observed from 8.348 Å for $\delta = 0.0$ to 8.285 Å for $\delta = 0.9$ for the $CoV_\delta Fe_{2-\delta}O_4$ nanomaterials. Detailed and precise observation revealed that when the V content was increased from $\delta = 0.0$ to $\delta = 0.1$, there was a slight increase in the lattice parameters values from 8.348 Å to 8.365 Å, respectively. Next, no measurable variation was found for $\delta = 0.3$. However, the values of the lattice parameters for $CoV_\delta Fe_{2-\delta}O_4$ showed a systematic decreasing trend from 8.361 Å to 8.285 Å for $\delta = 0.3$ to $\delta = 0.9$, respectively. These results agreed well with the similar trends in variation of the crystallite sizes and lattice parameters already reported for vanadium-doped cobalt ferrite systems.[26]

In nanocrystalline systems, broadening of the XRD peaks occurs owing to the following reasons: (i) occurrence of nano-sized crystallites and (ii) strain induced line broadening due to lattice defects and dislocations. As the total broadening is the sum of the size and strain broadening, the Williamson–Hall (WH) method is employed for the separation of the same.[30,31] Fig. 4 shows the WH plots for all the compositions of $CoV_\delta Fe_{2-\delta}O_4$ nanomaterials considered here. Specifically, $\beta\cos(\theta)$ *vs.* $4\sin(\theta)$ were plotted and fitted with linear fit functions. The fitted values of the slope and intercept represent the lattice strain 'ε' and $\beta\cos(\theta)$. The crystallite size (D) (in nm) was calculated using the formula $D = (0.9\lambda)/(\beta\cos(\theta))$. The simulated values of the positive lattice strains and the crystallite sizes obtained from the WH plots are provided in Table 1. There was a significant increase in the lattice strain from 1.34×10^{-3} for pure $CoFe_2O_4$ to 2.00×10^{-3} for $CoV_{0.9}Fe_{1.1}O_4$. Such a kind of increasing trend in the values of lattice strains as a result of the progressive increase in large-sized dopant atoms in the spinel crystal structure has previously been reported in earlier studies.[30,32] This shows the presence of tensile force in the $CoV_\delta Fe_{2-\delta}O_4$ lattice. It was observed that the crystallite sizes calculated with Scherrer's formula were relatively smaller compared to those calculated from the WH plots. These results can be rationalized as follows: Scherrer's method neglects the microstrain in the lattice that may originate from imperfections in the structure, whereas in the WH plot method, there is a separation of the instrumental and sample broadening effects in the calculation.

In Fig. 5(a)–(c), the values of the XRD peak intensity ratios, *i.e.* $I_{(422)}/I_{(400)}$, $I_{(220)}/I_{(400)}$, and $I_{(400)}/I_{(440)}$, are plotted against the vanadium content, δ, in $CoV_\delta Fe_{2-\delta}O_4$ ($0.0 \leq \delta \leq 0.9$). The observed drastic variation in the peak intensity ratios indicated cation distributions as a result of the increasing V content in the $CoFe_2O_4$ lattice. The intensity ratio $I_{(220)}/I_{(400)}$ decreased from 0.88 for $\delta = 0.0$ to 0.72 for $\delta = 0.3$, and then showed an increasing trend thereafter with a broad-hump peak at $\delta = 0.7$. Next, the peak intensity ratio of $I_{(422)}/I_{(400)}$ plotted against the V content, first showed an initial sharp decrease up to $\delta = 0.1$, *i.e.* from 0.61 for $\delta = 0.0$ to 0.51 for $\delta = 0.1$, then showed no measurable change from $\delta = 0.3$ to $\delta = 0.9$, for which the $I_{(422)}/I_{(400)}$ ratio was found to be 0.52. Finally, considering the ratio of $I_{(400)}/I_{(440)}$ as a function of V content, δ, there was an initial increase from 0.34 for $\delta = 0.0$ to 0.37 for $\delta = 0.1$, followed by an increasing trend, with a broad-hump peak at $\delta = 0.7$. These above-mentioned planes are known to be sensitive to the cation distribution between tetrahedral and octahedral holes in the spinel crystal lattice. Qualitatively, it could be anticipated that the alterations in the peak intensity ratios mentioned above may alter the magnetic structure of ferrite materials.[21,33]

 This journal is © The Royal Society of Chemistry and the Centre National de la Recherche Scientifique 2025

Open Access Article. Published on 18 November 2024. Downloaded on 5/8/2026 8:39:22 PM.
This article is licensed under a Creative Commons Attribution 3.0 Unported Licence.

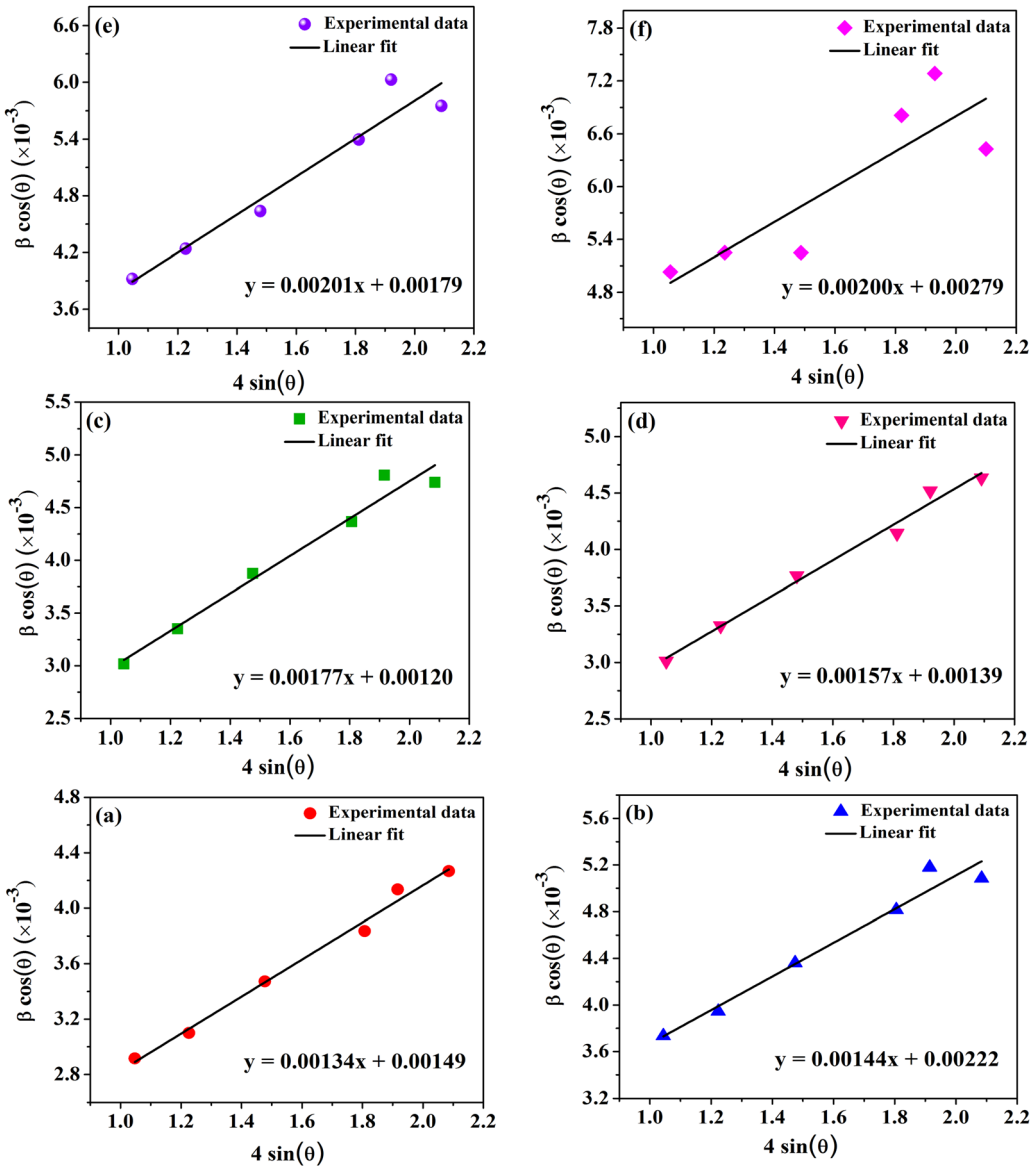

Fig. 4 Linearly fitted Williamson–Hall (WH) plots for $CoV_\delta Fe_{2-\delta}O_4$ ($0.0 \leq \delta \leq 0.9$) nanomaterials annealed at 700 °C for different vanadium contents, δ: (a) 0.0, (b) 0.1, (c) 0.3, (d) 0.5, (e) 0.7 and (f) 0.9.

3.2 FTIR spectroscopic analysis

Fig. 6 shows the FTIR spectra of the $CoV_\delta Fe_{2-\delta}O_4$ ($0.0 \leq \delta \leq 0.9$) nanomaterials recorded in the range of 4000–400 cm^{-1}. The presence of M–O bonding, where M stands for metal (M = Co (Fe/V)), was confirmed by the presence of strong peaks located in the frequency ranges of 409–420 cm^{-1} and 454–460 cm^{-1} for the octahedral (O_h) (ν_2) coordination, while the frequency range 589–603 cm^{-1} represented the tetrahedral (T_d) (ν_1) coordination.[34,35] As the nanomaterials were obtained *via* the autocombustion of citrate gel at elevated temperatures, in addition to the above-mentioned characteristics ν_2 and ν_1 bands for the spinel structure, a few low intensity peaks (compared to the intensity of the ν_2 and ν_1 bands) corresponding to organic linkages were observed. The IR bands located in the frequency ranges of 839–888 cm^{-1} and 952–962 cm^{-1} are the signature of M–O-organic linkages.[21,36] The IR peak near 1690 cm^{-1} was assigned to the carbonyl (C═O) group of citrate complexes. Also, the weak bands observed at 1545–1550 cm^{-1} and 1639–1641 cm^{-1} were assigned to M–(COO)-organic linkages.[21,36] The medium to strong IR band located near 2346 cm^{-1} was assigned due to the presence of adsorbed CO_2 and M–O–O-organic linkages.[16] The IR bands observed at nearly 3445 cm^{-1} in almost all the compositions were related to possible O–H stretching of the adsorbed H_2O (l).[21,37]

The variations in the IR frequencies corresponding to the octahedral and tetrahedral coordination for each composition of the $CoV_\delta Fe_{2-\delta}O_4$ ($0.0 \leq \delta \leq 0.9$) materials are presented in Fig. 7. For both coordinations, an initial decrease in the trend of ν_1 and ν_2 was observed down to a minimum at δ = 0.1.

Open Access Article. Published on 18 November 2024. Downloaded on 5/8/2026 8:39:22 PM.
This article is licensed under a Creative Commons Attribution 3.0 Unported Licence.

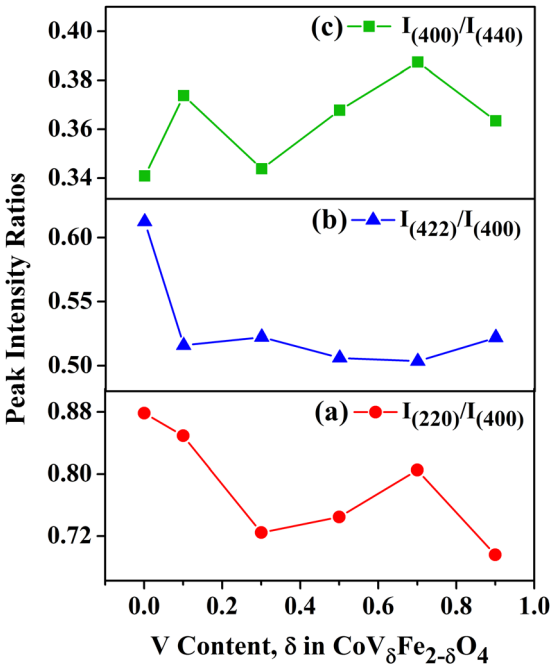

Fig. 5 XRD peak intensity ratios *vs.* vanadium content, δ, in $CoV_{\delta}Fe_{2-\delta}O_4$ ($0.0 \leq \delta \leq 0.9$) nanomaterials: (a) $I_{(220)}/I_{(400)}$, (b) $I_{(422)}/I_{(400)}$ and (c) $I_{(400)}/I_{(440)}$.

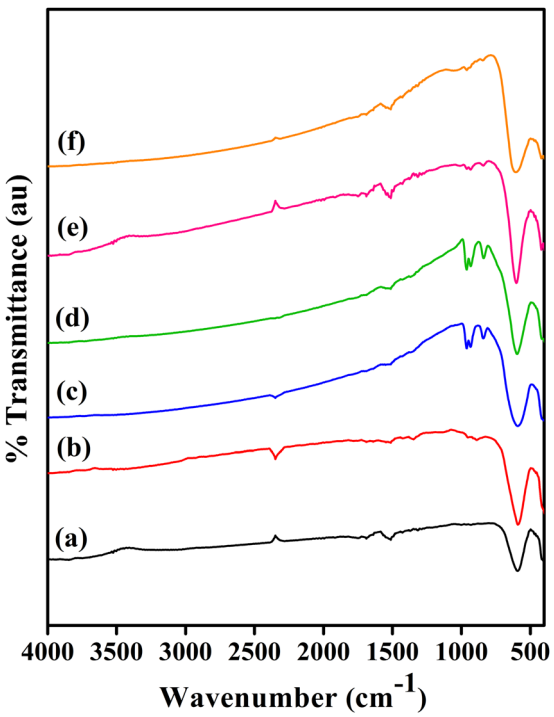

Fig. 6 FTIR spectra of $CoV_{\delta}Fe_{2-\delta}O_4$ nanomaterials annealed at 700 °C for different vanadium contents, δ: (a) 0.0, (b) 0.1, (c) 0.3, (d) 0.5, (e) 0.7 and (f) 0.9.

However, after attaining the minima, an increasing trend in the values of the ν_1 and ν_2 frequencies was then observed until

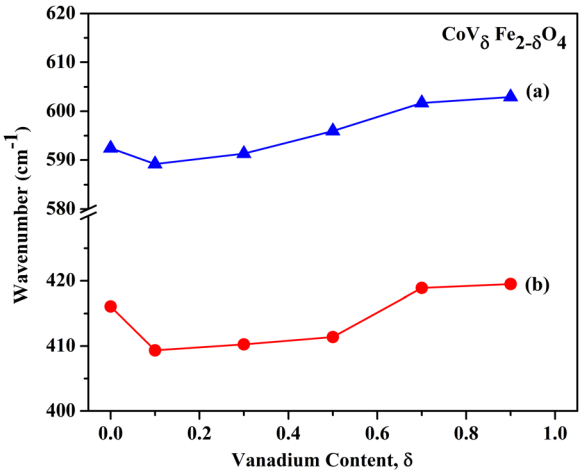

Fig. 7 Variation of IR frequencies as a function of vanadium content (δ) in $CoV_{\delta}Fe_{2-\delta}O_4$ ($0.0 \leq \delta \leq 0.9$) nanomaterials annealed at 700 °C for various coordination sites: (a) tetrahedral site and (b) octahedral site.

reaching a saturation value at $\delta = 0.9$. Thus, the number and nature of the metal ions that form bonds with oxygen in octahedral and tetrahedral coordinations were significantly with the progressive increase in vanadium (δ) content. These results, *i.e.* variation in the range of frequencies of ν_1 and ν_2, could be related to the cation distribution in the cobalt ferrite spinel lattice.[38]

3.3 Raman spectroscopy studies

The Raman spectra for the $CoV_{\delta}Fe_{2-\delta}O_4$ nanomaterials annealed at 700 °C are shown in Fig. 8. The characteristic Raman shifts for the $CoV_{\delta}Fe_{2-\delta}O_4$ nanomaterials with varying the vanadium content (δ) are summarized in Table 2. Vibrational modes showing the asymmetric stretching, symmetric stretching, and symmetric bending of the bonds associated with A site or B site cations in the spinel structure (AB_2O_4) and O^{2-} anions could be observed in the Raman spectra.[39,40] Factor group analysis was used to predict the number of active Raman modes in the cubic spinel having space group *Fd3m*; such as A_{1g}, E_g, and $3T_{2g}$. These modes are generated from the cations' M–O vibrations occurring in octahedral and tetrahedral sites. The alterations of the peak positions, broadening, and intensities can be correlated to cation redistribution in the $CoV_{\delta}Fe_{2-\delta}O_4$ nanomaterials.[41] The $CoV_{\delta}Fe_{2-\delta}O_4$ nanomaterials annealed at 700 °C showed Raman modes in the frequency ranges of 218 cm–229, 292–314, 454–472, 601–632, and 680–696 cm^{-1}, which were assigned to the $T_{2g}(3)$, $E_g(2)$, $T_{2g}(2)$, $A_{1g}(2)$, and $A_{1g}(1)$ modes, respectively.[42,43] Plots of the Raman peak intensity ratios, *i.e.* $A_{1g}(2)/A_{1g}(1)$ and $A_{1g}(2)/T_{2g}(2)$ *vs.* vanadium content, δ, in the $CoV_{\delta}Fe_{2-\delta}O_4$ ($0.0 \leq \delta \leq 0.9$) nanomaterials are shown in Fig. 9. The peak intensity ratio $A_{1g}(2)/T_{2g}(2)$ was considered to indicate the relative occupation of Co^{2+} in tetrahedral and octahedral sites; whereby a higher ratio indicates a lower degree of inversion in the structure, where more Co^{2+} ions migrate from octahedral to tetrahedral interstitials. Further, the intensity ratio $A_{1g}(2)/A_{1g}(1)$ can also be related to

 This journal is © The Royal Society of Chemistry and the Centre National de la Recherche Scientifique 2025

Open Access Article. Published on 18 November 2024. Downloaded on 5/8/2026 8:39:22 PM.
This article is licensed under a Creative Commons Attribution 3.0 Unported Licence.

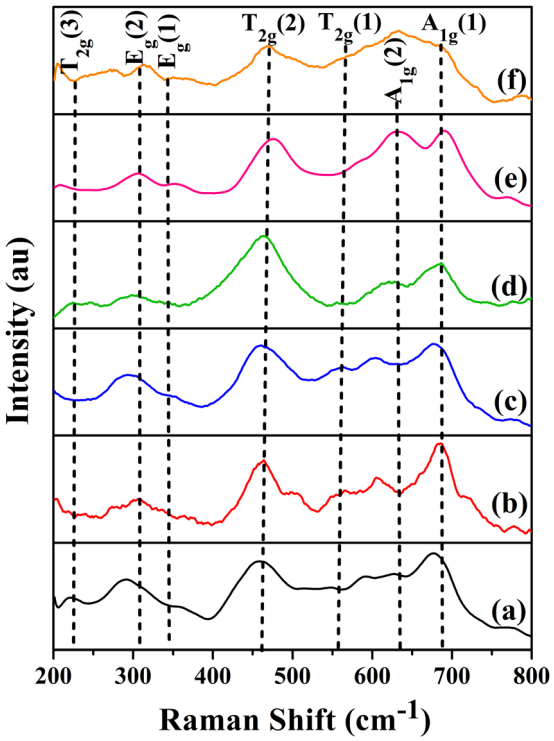

Fig. 8 Raman spectra for $CoV_\delta Fe_{2-\delta}O_4$ nanomaterials annealed at 700 °C for different vanadium contents, δ: (a) 0.0, (b) 0.1, (c) 0.3, (d) 0.5, (e) 0.7 and (f) 0.9.

the cation distribution; whereby a higher intensity ratio of $A_{1g}(2)/A_{1g}(1)$ indicates a smaller inversion degree, with Fe^{3+} ions majorly occupying the tetrahedral sites. The peak intensity ratio $A_{1g}(2)/T_{2g}(2)$ increase from 0.0148 to 0.2799 for $\delta = 0$ to $\delta = 0.9$, respectively, whereas for $[A_{1g}(2)/A_{1g}(1)]$, the increase was steeper, *i.e.* 0.0225 to 0.6395 for $\delta = 0$ to $\delta = 0.9$, respectively. Thus, with more and more V^{5+} insertion in the spinel lattice, the above-mentioned ratios increased, indicating a lower degree of inversion.

3.4 FESEM studies

FESEM micrographs were obtained and are presented in Fig. 10(a)–(f). The morphology and histograms for the particle-size distribution (inset) of the products annealed at 700 °C are shown in Fig. 10. Spherical shapes along with aggregated particles forming a trigonal bipyramidal morphology could be observed. The FESEM particle sizes are given in

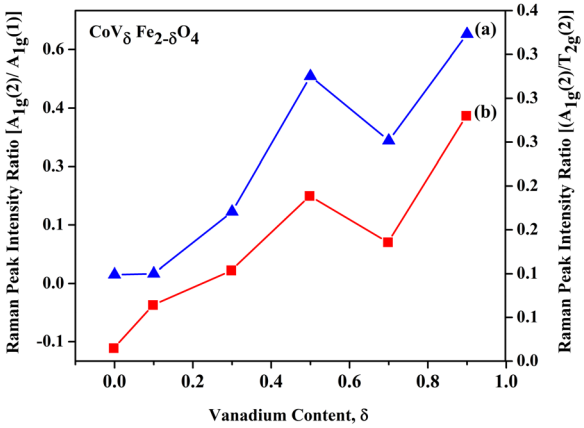

Fig. 9 Plots of Raman peak intensity ratios *vs.* vanadium content, δ, in $CoV_\delta Fe_{2-\delta}O_4$ ($0.0 \le \delta \le 0.9$) nanomaterials: (a) $A_{1g}(2)/A_{1g}(1)$ and (b) $A_{1g}(2)/T_{2g}(2)$.

Table 1. The FESEM micrographs depict anisotropic, polydispersed particles with the particle sizes of the $CoV_\delta Fe_{2-\delta}O_4$ materials varying from 56 nm to 34 nm for $\delta = 0.0$ down to $\delta = 0.9$, respectively. As can be seen from Table 1, the FESEM particle sizes agreed well with the crystallite sizes estimated from the WH plots. The presence of the elements, *i.e.* Co, Fe, V, and O, were confirmed by the EDS spectra, wherein the atomic percentages of these elements complied with the stoichiometry of the $CoV_\delta Fe_{2-\delta}O_4$ materials.

3.5 XPS studies

Fig. 11(a)–(d) present the XPS spectra for the chemical states of the various elements for the selected composition of $CoV_\delta Fe_{2-\delta}O_4$ nanomaterials, *i.e.* pure $CoFe_2O_4$ and $CoV_{0.5}Fe_{1.5}O_4$ are shown. The binding energy values were calibrated using the observed adventitious C1s peak at 284.8. The observed peaks (in Fig. 11) majorly corresponded to the $2p^{3/2}$ and $2p^{1/2}$ states of Co^{2+}, Fe^{3+}, and V^{5+} ions, as well as the 1s states of the O^{2-} ion. The changes in peak positions and intensities of the Co-$2p^{3/2}$ and Fe-$2p^{3/2}$ spectra corresponding to both their tetrahedral and octahedral coordination were analyzed and compared. Fig. 11(a) shows the distinct peaks corresponding to Co^{2+} ions in tetrahedral and octahedral environments were located at 782.1 and 779.5 eV (with an intensity ratio of $\approx 1:1$) for $CoFe_2O_4$, respectively. For the $CoV_{0.5}Fe_{1.5}O_4$ materials, peak positions of 780.4 and 779.32 eV (with an intensity ratio

Table 2 Characteristic Raman shifts for $CoV_\delta Fe_{2-\delta}O_4$ nanomaterials for different values of vanadium content (δ), along with the peak intensity ratios $[A_{1g}(2)/A_{1g}(1)]$ and $[A_{1g}(2)/T_{2g}(2)]$

	Raman shift (cm^{-1})						Peak intensity ratios	
V content, δ ($CoV_\delta Fe_{2-\delta}O_4$)	$T_{2g}(3)$	$E_g(2)$	$E_g(1)$	$T_{2g}(2)$	$A_{1g}(2)$	$A_{1g}(1)$	$[A_{1g}(2)/A_{1g}(1)]$	$[A_{1g}(2)/T_{2g}(2)]$
0.0	222	292	354	454	626	681	0.0225	0.0148
0.1	218	306	355	458	606	680	0.0251	0.0642
0.3	229	294	351	461	601	683	0.1839	0.1036
0.5	222	295	350	460	613	684	0.532	0.1886
0.7	225	306	338	472	632	696	0.3662	0.1356
0.9	226	314	339	468	629	693	0.6395	0.2799

Open Access Article. Published on 18 November 2024. Downloaded on 5/8/2026 8:39:22 PM.
This article is licensed under a Creative Commons Attribution 3.0 Unported Licence.

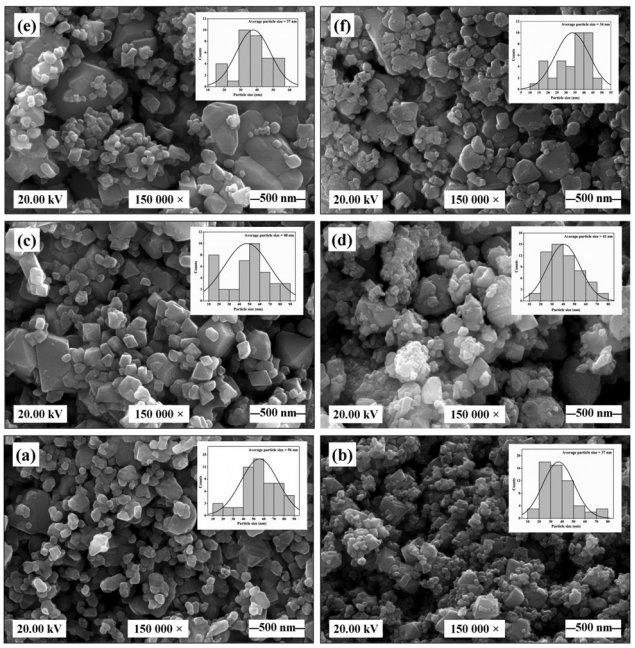

Fig. 10 FESEM micrographs for $CoV_\delta Fe_{2-\delta}O_4$ nanomaterials annealed at 700 °C for different vanadium contents, δ: (a) 0.0, (b) 0.1, (c) 0.3, (d) 0.5, (e) 0.7 and (f) 0.9 (insets present histograms of particle-size distributions in the respective $CoV_\delta Fe_{2-\delta}O_4$ nanomaterials).

of $\approx 5.3:1$) were observed for Co^{2+} ions in tetrahedral (T_d) and octahedral (O_h) environments, respectively. These results indicate the increase in Co^{2+} ion concentrations in the tetrahedral environment as a result of vanadium ion incorporation in the $CoFe_2O_4$ material. In a similar manner, Fig. 11(b) shows distinct peaks corresponding to Fe^{3+} ions in T_d and O_h environments at 711.2 and 709.8 eV (with an intensity ratio of $\approx 1:2$) for $CoFe_2O_4$, respectively. For the $CoV_{0.5}Fe_{1.5}O_4$ materials, peaks were observed located at 712.4 and 709.5 eV (with an intensity ratio of $\approx 0.8:1$) for Fe^{3+} ions in T_d and O_h environments, respectively.[39,44] In addition, we observed a small intensity peak at 707 eV for the vanadium-substituted product, which was attributed to the occurrence of the Fe^{2+} state in the material. The above results indicate the increase in Fe^{3+} concentration in the tetrahedral coordination. In the O1s spectrum, peaks corresponding to lattice oxygen and molecular oxygen were observed at binding energy values of 529.9 and 532.3 eV, respectively (Fig. 11(c)). The observation of two distinct peaks at binding energy values of 516.1 and 517.7 eV corresponded to V^{4+} and V^{5+} states, respectively.[45] The existence of the V^{4+} state in the materials along with V^{5+} and the redistribution of Co^{2+} and Fe^{3+} ions in the octahedral and tetrahedral coordination confirmed the redistribution of cations as a result of vanadium incorporation.

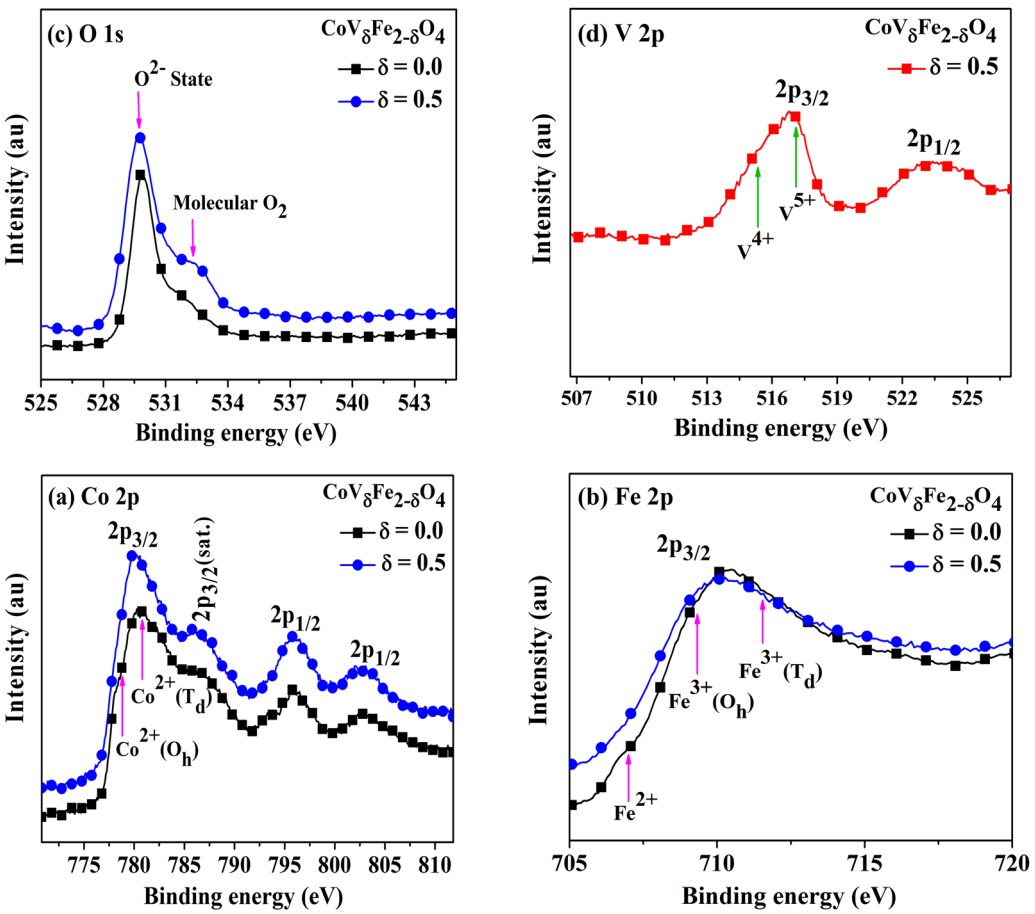

Fig. 11 XPS spectra of $CoV_\delta Fe_{2-\delta}O_4$ nanomaterials (annealed at 700 °C) for (a) Co-2p, (b) Fe-2p, (c) O-1s for δ = 0 and (d) V-2p for δ = 0.5.

 This journal is © The Royal Society of Chemistry and the Centre National de la Recherche Scientifique 2025

Open Access Article. Published on 18 November 2024. Downloaded on 5/8/2026 8:39:22 PM.
This article is licensed under a Creative Commons Attribution 3.0 Unported Licence.

Table 3 Materials composition (δ), saturation magnetization (M_s), coercivity (H_c), remanent magnetization (M_r), squareness ratio (M_r/M_s), magnetocrystalline anisotropic constant (K_1), effective magnetic anisotropic constant (K_{eff}) and surface anisotropy (K_s) measured at room temperature (300 K) for $CoV_\delta Fe_{2-\delta}O_4$ nanomaterials (annealed at 700 °C)

Material composition, δ ($CoV_\delta Fe_{2-\delta}O_4$)	Saturation magnetization, M_s (emu g^{-1})	Coercivity, H_c (Oe)	Remanent magnetization, M_r (emu g^{-1})	Squareness ratio (M_r/M_s)	K_1 (J m^{-3}) ($K_1 \times 10^4$)	K_{eff} (J m^{-3}) ($K_{eff} \times 10^4$)	K_s (J m^{-2}) ($K_s \times 10^{-3}$)
$\delta = 0.0$	82.5	1180	36.3	0.4402	1.44	1.521	70.2
$\delta = 0.1$	74.5	1151	33.2	0.4451	1.32	1.339	12.35
$\delta = 0.3$	71.1	1065	31.6	0.4444	1.39	1.118	−22.213
$\delta = 0.5$	68.1	885	30.6	0.4501	1.26	0.9416	−25.472
$\delta = 0.7$	56.9	946	21.3	0.3740	1.22	0.8410	−24.003
$\delta = 0.9$	47.3	886	17.1	0.3624	1.19	0.6548	−26.76

3.6 Magnetic properties of $CoV_\delta Fe_{2-\delta}O_4$ nanomaterials ($0.0 \leq \delta \leq 0.9$)

3.6.1 Room-temperature magnetic properties. Fig. 12 presents the of *M–H* hysteresis curves for $CoV_\delta Fe_{2-\delta}O_4$ nanomaterials recorded at room temperature (300 K). The values of saturation magnetization (M_s) were estimated using the fitted data obtained from the plot of ($1/H^2$) *vs.* magnetization (M), where H is the applied field strength. The values of the saturation magnetization (M_s), coercivity (H_c) and remanent magnetization (M_r) at room temperature (300 K) for $CoV_\delta Fe_{2-\delta}O_4$ are summarized in Table 3. The values of M_s were estimated to be 82.5, 74.5, 71.1, 68.1, 56.9, and 47.3 emu g^{-1} for vanadium contents δ = 0.0, 0.1, 0.3, 0.5, 0.7, and 0.9, respectively. Similarly, the values of H_c obtained from the *MH* curve were 1180, 1151, 1065, 885, 946, and 886 Oe for V contents δ = 0.0, 0.1, 0.3, 0.5, 0.7, and 0.9, respectively. The values of M_s and coercivity (H_c) were plotted against the increasing content of vanadium 'δ' in $CoV_\delta Fe_{2-\delta}O_4$ (where δ = 0.0, 0.1, 0.3, 0.5, 0.7, 0.9), as depicted in Fig. 13. As can be observed from the plot, the variation in the values of M_s followed a systematic linear decrease from 82.5 emu g^{-1} down to 47.3 emu g^{-1} for δ = 0.0 and δ = 0.9, respectively. Similarly, a linear decrease in the values of H_c was observed, *i.e.* from 1180 Oe to 886 Oe for δ = 0.0 to δ = 0.9, respectively, besides the drastic decrease in the H_c value to 946 Oe at δ = 0.7.

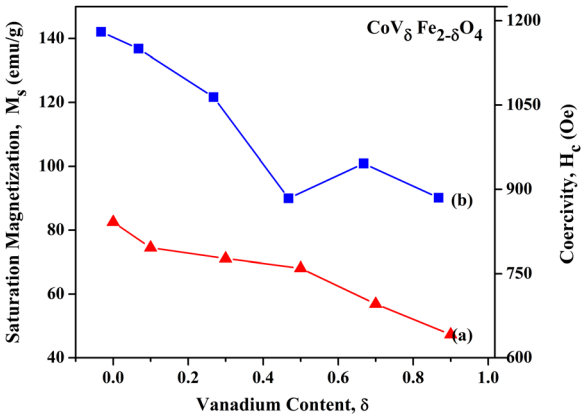

Fig. 13 Variation in magnetic parameters at room temperature (300 K) for $CoV_\delta Fe_{2-\delta}O_4$ ($0.0 \leq \delta \leq 0.9$) nanomaterials: (a) saturation magnetization (M_s) and (b) coercivity (H_c).

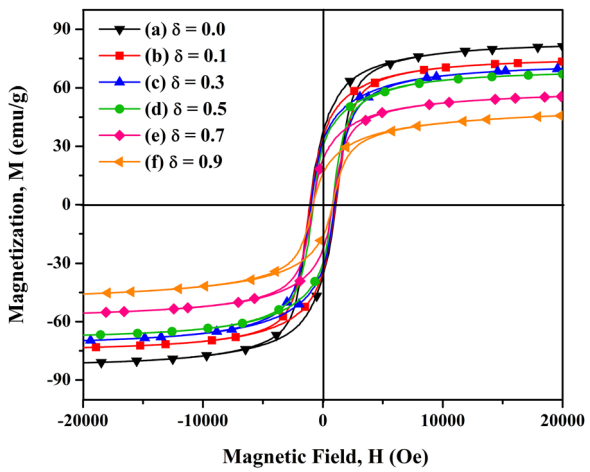

Fig. 12 Plots of *M vs. H* (measured at 300 K) for $CoV_\delta Fe_{2-\delta}O_4$ nanomaterials annealed at 700 °C for different vanadium contents, δ: (a) 0.0, (b) 0.1, (c) 0.3, (d) 0.5, (e) 0.7 and (f) 0.9.

In spinel ferrites, magnetization originates from the vector sum of two unequal magnetic sublattices (A and B) arranged in an antiparallel manner.[46–48] In the lattice structure, three kinds of interactions exist, namely: A–A, A–B, and B–B. The interatomic A–B super-exchange interactions are dominant over A–A and B–B interactions. In particular, in the inverse spinel $CoFe_2O_4$ system, the spins of Fe^{3+} at octahedral sites can be aligned antiparallel to the spins of Fe^{3+} at tetrahedral sites' whereas the Co^{2+} spins remain aligned to Fe^{3+} at octahedral sites.[17,49,50] Substitution of a transition metal ion M^{n+} in place of an Fe^{3+} ion octahedral site can result in the redistribution of Co^{2+} in the tetrahedral and octahedral sites and a possible change in the degree of inversion in such materials.[51] It has been observed that magnetization may first increase to a maximum value and then decrease as a result of metal ion substitution. This behaviour of an initial increase of magnetization and subsequent decrease can be attributed to the degree of inversion and weakening of the A–B superexchange interactions as a result of metal ion incorporation, respectively. The overall magnetic properties of $CoV_\delta Fe_{2-\delta}O_4$ nanomaterials depend on several factors, such as (i) cation distribution in the octahedral and tetrahedral sites, (ii) extent to which vanadium substitution occurs, (iii) shape, size, and surface effects,

Open Access Article. Published on 18 November 2024. Downloaded on 5/8/2026 8:39:22 PM. This article is licensed under a Creative Commons Attribution 3.0 Unported Licence.

(iv) lattice strain, (v) magnetic nature of V substituent, and (vi) spin canting.[12,52]

The extent of the magnetic interactions depends on the inter-ionic separations and the angle between them.[53] When V^{5+} is substituted in spinel ferrites, due to difference in ionic radii, the inter-ionic separations may change. This leads to an alteration of the magnetization of the materials. In addition, V^{5+} ions, having no d-orbital electrons, do not contribute towards the spin only magnetic moment of the sample, directly. However, the existence of V^{4+} in the material cannot be ruled out and XPS investigation supported its existence (Section 3.5). The substitution of V^{5+} in place of Fe^{3+} promoted a redistribution of the cations in the interstitial sites, as proven by our XPS study. To be noted, the research approach for this kind of idea has been tested successfully by substituting aliovalent dopants in $BaSnO_3$ oxide material systems.[6] Also, Co^{2+} can migrate from tetrahedral to octahedral interstitial sites, whereas varied fractions of Fe^{3+} can distribute themselves in suitable octahedral and tetrahedral positions. In addition, the presence of a minute quantity of Fe^{2+} ions can also contribute towards the magnetization. Because of the fact that Fe^{3+} ions situated in two different environments (O_h and T_d) have differences in their intrinsic magnetic moments, the above-mentioned cation redistribution effect can lead to a significant change in the magnetization. The increasing trend in the plot of the Raman peak intensity ratios *vs.* vanadium content, y, in the $CoV_\delta Fe_{2-\delta}O_4$ ($0.0 \leq \delta \leq 0.9$) nanomaterials, *i.e.* $A_{1g}(2)/A_{1g}(1)$ and $A_{1g}(2)/T_{2g}(2)$, proved the above arguments (see Fig. 9). Such analysis of the cation redistribution leading to an alteration of the net magnetic moment has already been proven in ferromagnetic systems.[40,52,54] In addition, the $CoV_\delta Fe_{2-\delta}O_4$ ($0.0 \leq \delta \leq 0.9$) nanomaterials studied in this research work for assessing their magnetic properties are nano-structured in nature, where size, strain, and surface effects, including spin canting, can substantially reduce the net magnetization.[55,56] The above-mentioned factors explain the nearly linear decrease of M_s from 82.5 emu g^{-1} down to 47.3 emu g^{-1} with the increase in vanadium content, δ, in $CoV_\delta Fe_{2-\delta}O_4$ from $\delta = 0.0$ to $\delta = 0.9$, respectively. In a similar manner, the above inferences are strengthened by reports showing a drastic decrease in values of M_s observed in the Nb^{5+}-doped NiZnCo ferrite system.[57]

The coercivity (H_c) for nanometre-scale ferrite materials can be expressed as:

$$H_c = 3[(kT_cK_1/aM_s)][(1/D)],$$

where T_c is the Curie temperature, K_1 is the first anisotropy constant, 'a' is a lattice parameter, M_s is the saturation magnetization, and 'D' is the grain diameter.[58] The observed decrease in coercivities from 1180 Oe to 886 Oe for $\delta = 0.0$ to $\delta = 0.9$, respectively, in $CoV_\delta Fe_{2-\delta}O_4$ ($0.0 \leq \delta \leq 0.9$) could not be due to the increase in M_s and/or increase in grain diameter as per the above-mentioned expression. To be noted, M_s and the grain size decreased with the continuous increase in vanadium substitution in $CoV_\delta Fe_{2-\delta}O_4$ ($0.0 \leq \delta \leq 0.9$). Therefore, the decrease in coercivity can be majorly related to the reduction in the magnetic anisotropy constant with the increase in vanadium atom substitution in the $CoV_\delta Fe_{2-\delta}O_4$ ($0.0 \leq \delta \leq 0.9$) nanomaterials.[21] These observations were confirmed by estimations of the magnetocrystalline anisotropy constant (K_1), effective magnetic anisotropy constant (K_{eff}), and surface anisotropy (K_s) at 300 K.[59–61] The values of K_1 were estimated from the expression $K_1 = M_s \times \sqrt{\frac{105 \times b}{8}}$, where M_s and the 'b' factor were obtained from linear fitting of the M *vs.* $(1/H^2)$ plot, which followed the expression $M = M_s\left(1 - \frac{b}{H^2}\right)$.[59,61] The values of K_1 showed a decreasing trend, *i.e.* from 1.44×10^4 to 1.19×10^4 J m^{-3} for $\delta = 0.0$ to $\delta = 0.9$, respectively (Table 3). The values of K_{eff} were estimated using the expression $K_{eff} = \frac{H_c \times M_s}{0.64}$ (Table 3). The calculated values of K_{eff} were in the range of 1.521×10^4 to 6.548×10^3 J m^{-3} for $\delta = 0.0$ to $\delta = 0.9$, respectively. Similarly, the values of K_s were obtained using the expression $K_{eff} = K_1 + \frac{6K_s}{D'}$ where D' is the diameter of the crystallite (Table 3). It is clear from Table 3 that the K_s values varied significantly from 70.2×10^{-3} to 12.35×10^{-3} J m^{-2} for $\delta = 0.0$ to $\delta = 0.1$, respectively. The K_s values were found to be negative for $\delta = 0.3$ to $\delta = 0.9$, indicating different stress directions with respect to the magnetization axis. The squareness ratio increased initially from 0.4402 for $\delta = 0.0$ until it reached a maximum value of 0.4501 for $\delta = 0.5$, and thereafter showed a decreasing trend down to 0.3624 for $\delta = 0.9$. For the $CoV_\delta Fe_{2-\delta}O_4$ ($0.0 \leq \delta \leq 0.9$) nanomaterials, the M_r/M_s values were found to be in the range of 0.4501–0.3624 (Table 3). These results can be explained by the possible existence of a surface spin canting effect as a consequence of the nanoparticle size and surface effects.[62]

3.6.2 Low-temperature magnetic properties. The M *vs.* H curves were recorded at low temperature, *i.e.* at 5 K, for $CoV_\delta Fe_{2-\delta}O_4$ nanomaterials and are presented in Fig. 14. The M *vs.* H plots indicated the nanomaterials had ferrimagnetic

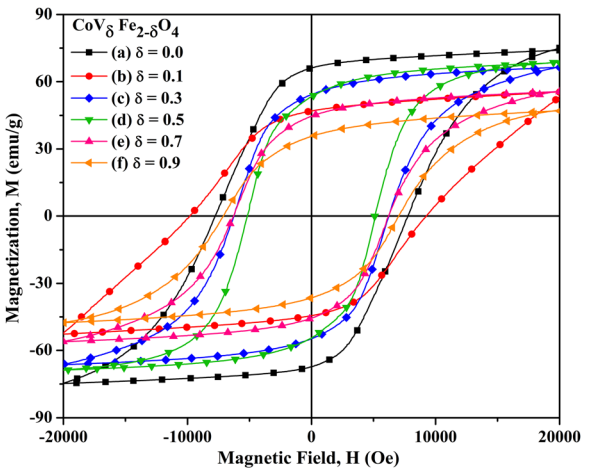

Fig. 14 M *vs.* H plots (measured at 5 K) for $CoV_\delta Fe_{2-\delta}O_4$ nanomaterials annealed at 700 °C for different contents of vanadium, δ: (a) 0.0, (b) 0.1, (c) 0.3, (d) 0.5, (e) 0.7 and (f) 0.9.

 This journal is © The Royal Society of Chemistry and the Centre National de la Recherche Scientifique 2025

Open Access Article. Published on 18 November 2024. Downloaded on 5/8/2026 8:39:22 PM. This article is licensed under a Creative Commons Attribution 3.0 Unported Licence.

Table 4 Material compositions, M_s, H_c, and M_r recorded at 5 K, squareness ratio (M_r/M_s), magnetocrystalline anisotropic constant (K_1), effective magnetic anisotropic constant (K_{eff}) and surface anisotropy (K_s) of $CoV_\delta Fe_{2-\delta}O_4$ nanomaterials

Material composition, δ ($CoV_\delta Fe_{2-\delta}O_4$)	Saturation magnetization, M_s (emu g^{-1})	Coercivity, H_c (Oe)	Remanent magnetization, M_r (emu g^{-1})	Squareness ratio (M_r/M_s)	K_1 (J m^{-3}) ($K_1 \times 10^4$)	K_{eff} (J m^{-3}) ($K_{eff} \times 10^4$)	K_s (J m^{-2}) ($K_s \times 10^{-5}$)
$\delta = 0.0$	74.8	7772	66.2	0.885	1.4254	9.0835	66.3702
$\delta = 0.1$	57.5	9538	46.9	0.816	1.4882	8.5692	46.0265
$\delta = 0.3$	67.9	6252	54.2	0.798	1.4396	6.6329	42.41195
$\delta = 0.5$	70.0	5150	53.4	0.763	1.4167	5.6328	33.7288
$\delta = 0.7$	57.3	6243	44.7	0.780	1.3276	5.5894	26.9914
$\delta = 0.9$	48.9	7078	35.7	0.730	1.2945	5.4080	20.5675

structures with large coercivities. With the increase in 'V' content in $CoV_\delta Fe_{2-\delta}O_4$, the values of M_s and H_c were found to alter quite significantly. The variation of the magnetic parameters, *i.e.* saturation magnetization (M_s) and coercivity (H_c), for the $CoV_\delta Fe_{2-\delta}O_4$ nanomaterials are shown in Fig. 15. Also, the values of M_s, H_c, and M_r, recorded at 5 K and estimated K_1, K_{eff}, K_s and squareness ratio (M_r/M_s) for various values of δ in $CoV_\delta Fe_{2-\delta}O_4$ are summarized in Table 4.

The M_s values obtained from the fitted data obtained from the plot of $(1/H^2)$ *vs.* magnetization (M) for the $CoV_\delta Fe_{2-\delta}O_4$ nanomaterials varied from 74.8 to 48.9 emu g^{-1} for $\delta = 0.0$ to $\delta = 0.9$, respectively. The decrease in M_s as a function of the V content 'δ' has already been explained in subsection 3.5.1. As can be observed from the M *vs.* H plots, measured at 5 K, the approach towards saturation of the magnetization was quite flat compared with those recorded at a temperature of 300 K. These results can be rationalized due to superferromagnetic phase transition occurring at lower temperatures. Also, the variation in the values of H_c was observed to vary from 7772 to 7078 Oe for $\delta = 0.0$ to $\delta = 0.9$, respectively. The $CoV_\delta Fe_{2-\delta}O_4$ nanomaterials showed a significant increase in coercivity from 7772 Oe ($\delta = 0.0$) to 9538 Oe ($\delta = 0.1$). This observation of large coercivity may be explained on the basis of the larger magnetocrystalline anisotropy (K_1) for $CoV_{0.1}Fe_{1.9}O_4$ (Table 4), and the alterations in the size, shape, and surface effects.[63,64] The estimated values of K_1 showed a decreasing trend, *i.e.* from 1.42×10^4 to 1.29×10^4 J m^{-3} for $\delta = 0.0$ to $\delta = 0.9$, respectively (Table 4). The calculated values of K_{eff} were in the range of 9.08×10^4 to 5.40×10^4 J m^{-3} for $\delta = 0.0$ to $\delta = 0.9$, respectively. It can be seen from Table 4 that the K_s values varied from 66.37×10^{-5} to 20.56×10^{-5} J m^{-2} for $\delta = 0.0$ to $\delta = 0.9$, respectively. The decreasing value of the magnetic anisotropy constant as a result of vanadium incorporation supports the observed decreasing trend for H_c. Alterations of the crystallite size and particle morphology in the $CoV_\delta Fe_{2-\delta}O_4$ nanomaterials as a function of the increasing vanadium content can be a major reason for the reduction of H_c. In addition, the nanomaterials synthesized by the current method displayed a superparamagnetic nature at 300 K. At lower temperatures, magnetocrystalline anisotropy dominated over the thermal energy, kT, whereby a large increase in H_c values could be seen with the single domain particles.[12] It could also be noted that M_r showed a significant change as the V content increased in the cobalt ferrite lattice, with M_r observed to change from 66.2 to 35.7 emu g^{-1} for $\delta = 0.0$ to $\delta = 0.9$, respectively. Drastic variations in the values of M_r were observed from 66.2 emu g^{-1} for $\delta = 0.0$ to 46.9 emu g^{-1} for $\delta = 0.1$ in the $CoV_\delta Fe_{2-\delta}O_4$ nanomaterials. For the compositions $\delta = 0.3$ and $\delta = 0.5$, there was no significant change observed in the values of M_r, whereas for $\delta = 0.7$ and $\delta = 0.9$, the remanent magnetisation varied from 44.7 to 35.7 emu g^{-1}, respectively. These values of remanent magnetization suggest uniaxial anisotropy of the nanoparticles, which is also strongly depended on the shapes and sizes of the nanomaterials.[65] The squareness ratios were all significantly high and varied from 0.885 for $\delta = 0.0$ to 0.730 for $\delta = 0.9$ (Table 4 and Fig. 15).

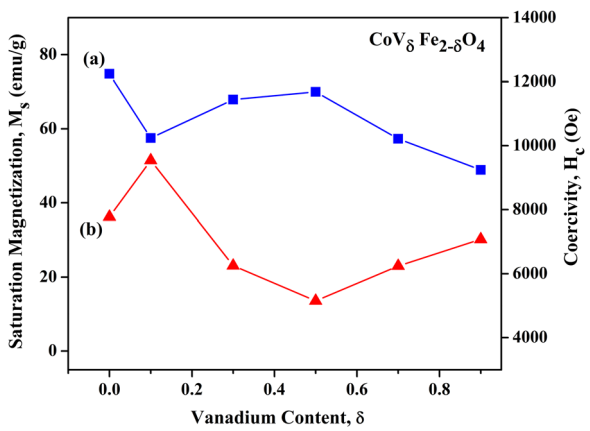

Fig. 15 Plots of the variation in (a) M_s and (b) H_c measured at 5 K for various V contents, δ = 0.0, 0.1, 0.3, 0.5, 0.7 and 0.9 in $CoV_\delta Fe_{2-\delta}O_4$ nanomaterials.

Finally, the observed magnetic parameters for one of the compositions of cobalt ferrites ($CoV_{0.1}Fe_{1.9}O_4$) in the present work and those of some literature reported results are compared in Table 5, demonstrating that our system could succeed in getting larger values of coercivities, *i.e.* 1151 Oe and 9538 Oe at 300 K and 5 K, respectively.

4. Conclusions

The synthesis of vanadium-substituted cobalt ferrite nanomaterials ($CoV_\delta Fe_{2-\delta}O_4$) *via* a citric acid-assisted sol–gel autocombustion method was carried out successfully at a relatively low temperature (400 °C). We successfully synthesized nanocrystalline pure-phase products with cubic spinel structures. The observed average values of the crystallite sizes varied from 43 nm ($\delta = 0.0$) to 25 nm ($\delta = 0.9$) for the $CoV_\delta Fe_{2-\delta}O_4$

Table 5 Comparison of some reported $CoV_{0.1}Fe_{1.9}O_4$ nanomaterials with respect to their synthesis methods, average crystallite size, saturation magnetization and coercivity measured at room temperature and at low temperature

Composition of material	Synthesis method	Annealing temperature (°C)/time (h)	Average crystallite size (nm)	Room temperature (298 K) magnetic properties		Low temperature (5 K) magnetic properties	
				M_s (emu g^{-1})	H_c (Oe)	M_s (emu g^{-1})	H_c (Oe)
$CoV_{0.1}Fe_{1.9}O_4$ (ref. 26)	Sol–gel auto-combustion	550 °C/3 h	27	68.30	1451	—	—
$CoV_{0.1}Fe_{1.9}O_4$ (ref. 27)	Sol–gel method	700 °C/1 h	23	69.85	1248.2	—	—
$Co_{0.9}V_{0.1}Fe_2O_4$ (ref. 51)	Sol–gel method	800 °C/3 h	35.8	60.6	859.7	—	—
$CoV_{0.1}Fe_{1.9}O_4$ (this work)	Sol–gel method	700 °C/3 h	34	74.5	1151	57.5	9538

Open Access Article. Published on 18 November 2024. Downloaded on 5/8/2026 8:39:22 PM.
This article is licensed under a Creative Commons Attribution 3.0 Unported Licence.

nanomaterials. The values of lattice strain calculated from WH plots varied from 1.34×10^{-3} to 2.00×10^{-3} for $\delta = 0.0$ to $\delta = 0.9$, respectively. A significant decrease in the lattice parameters was noted from 8.348 Å to 8.285 Å for $\delta = 0.0$ to $\delta = 0.9$, respectively proving the lattice contraction in the materials with the higher content of vanadium in the lattice. These results indicate the successful insertion of V^{5+} in the spinel ferrite crystal structure. FESEM micrographs confirmed the nature of the spherical-shaped particles with narrow size distributions and average particle sizes varying from 56 nm to 34 nm for $\delta = 0.0$ to $\delta = 0.9$, respectively. The formation of M–O bonds was indicated by the occurrence of bands in the frequency ranges of 589.2–602.9 cm^{-1} and 409.3–419.5 cm^{-1} for the tetrahedral and octahedral sites, respectively. Raman spectroscopic studies confirmed the various sites occupancy and degree of inversion. The values of the Raman peak intensity ratios, *i.e.* $A_{1g}(2)/A_{1g}(1)$ and $A_{1g}(2)/T_{2g}(2)$, *vs.* vanadium content, δ, in $CoV_\delta Fe_{2-\delta}O_4$ ($0.0 \leq \delta \leq 0.9$) were used to verify the Co^{2+} occupancy, which can affect degree of inversion. XPS studies confirmed the existence of Fe^{2+} and V^{4+} states in the ferrite samples. Further, the existence of the V^{5+} state and redistribution of Co^{2+} and Fe^{3+} ions in the Oh and Td coordination evidenced the cation redistribution as a result of vanadium ion incorporation in a continuous manner. These results correlated with the observed decreasing trend in M_s values in the $CoV_\delta Fe_{2-\delta}O_4$ ($0.0 \leq \delta \leq 0.9$) materials with the increase in vanadium content. The hysteresis curves recorded at 300 K showed a systematic decreasing trend for saturation magnetization (M_s), *i.e.* from 82.5 to 47.3 emu g^{-1} for $\delta = 0.0$ to $\delta = 0.9$, respectively. Similarly, the values of M_s measured at 5 K varied from 74.8 to 48.9 emu g^{-1} for $\delta = 0.0$ to $\delta = 0.9$, respectively. The observed magnetic properties could be explained by the following factors: (i) cation distribution, (ii) substitution of 'V', (iii) lattice strain, (iv) shape, size, and surface effects, (vi) canted spin structure, *etc.* The values of coercivity recorded at 300 K showed a marginal decrease from 1180 to 886 Oe for $\delta = 0.0$ to $\delta = 0.9$, respectively. Also, at a low temperature of 5 K, alterations of H_c were observed, *i.e.* from 7772 to 7078 Oe for $\delta = 0.0$ to $\delta = 0.9$, respectively. The observation of a large coercivity of 9538 Oe for $\delta = 0.1$ may be due to the occurrence of larger magnetocrystalline anisotropy in the sample. The overall decreasing trend in coercivity of the materials was correlated with the decreasing values of magnetocrystalline anisotropy as a result of the progressive increase in vanadium substitution in the $CoFe_2O_4$ materials. Also, there were significant changes in the values of M_r recorded at room temperature, which was observed to vary from 36.3 for $\delta = 0.0$ to 17.1 emu g^{-1} for $\delta = 0.9$, respectively in $CoV_\delta Fe_{2-\delta}O_4$. A variation in M_r/M_s ratios was observed from 0.4402 for $\delta = 0.0$ up to a maximum value of 0.4501 for $\delta = 0.5$ in $CoV_\delta Fe_{2-\delta}O_4$. Similarly, the values of M_r at 5 K changed from 66.2 for $\delta = 0.0$ to 35.7 emu g^{-1} for $\delta = 0.9$. The observed variations in the M_r/M_s ratio at 5 K (*i.e.* from 0.885 for $\delta = 0.0$ to 0.730 for $\delta = 0.9$) were quite significant for the nanomaterials for potential use in data-storage applications.

Author contributions

Anagha B. Patil: conceptualization, data curation, formal analysis, investigation, methodology, writing – original draft and writing – review and editing, Rabi N. Panda: conceptualization, methodology, supervision, writing – review and editing.

Data availability

The data that support the findings of this study are available within the paper and additional data will be made available upon request.

Conflicts of interest

There are no conflicts to declare.

Acknowledgements

We are thankful to the Central Sophisticated Instrumentation Facility (CSIF), BITS Pilani KK Birla Goa Campus for the provision of XRD, FESEM and Raman Spectroscopy data procurements. We also thank the Department of Physics, BITS PILANI K K Birla Goa Campus and Department of Science and Technology (DST), Government of India for Department of Science and Technology Funds for Improvement of Science and Technology (DST-FIST) grant number SR/FST/PS-I/2017/21 for PPMS VSM measurements. The authors would also like to acknowledge the central analytical laboratory at BITS Pilani, Hyderabad Campus for XPS measurements. One of the authors, Anagha B. Patil is thankful for the SRF fellowship to BITS Pilani University, Pilani India.

 This journal is © The Royal Society of Chemistry and the Centre National de la Recherche Scientifique 2025

Open Access Article. Published on 18 November 2024. Downloaded on 5/8/2026 8:39:22 PM. This article is licensed under a Creative Commons Attribution 3.0 Unported Licence.

References

1 M. Amiri, M. Salavati-Niasari and A. Akbari, Magnetic nanocarriers: Evolution of spinel ferites for medical applications, *Adv. Colloid Interface Sci.*, 2019, **265**, 29–44.

2 H. Qin, Y. He, P. Xu, D. Huang, Z. Wang, H. Wang, Z. Wang, Y. Zhao, Q. Tian and C. Wang, Spinel ferrites (MFe_2O_4): Synthesis, improvement and catalytic application in environment and energy field, *Adv. Colloid Interface Sci.*, 2021, **294**, 102486.

3 P. Thakur, S. Taneja, D. Chahar, B. Ravelo and A. Thakur, Recent advances on synthesis, characterization and high frequency applications of Ni–Zn ferrite nanoparticles, *J. Magn. Magn. Mater.*, 2021, **530**, 167925.

4 T. N. Pham, T. Q. Huy and A. T. Le, Spinel ferrite (AFe_2O_4)-based heterostructured designs for lithium-ion battery, environmental monitoring, and biomedical applications, *RSC Adv.*, 2020, **10**, 31622–31661.

5 W. Sharmoukh and S. M. Yakout, New spin-electronics compositions: Large ferromagnetic order of $BaSn_{0.98-x}Fe_{0.02}Cu_xO_3$ (x = 0.02, 0.04, 0.06) semiconductor, *J. Alloys Compd.*, 2024, **993**, 174664.

6 W. Sharmoukh, T. A. Hameed and S. M. Yakout, New nonmagnetic aliovalent dopants (Li^+, Cu^{2+}, In^{3+} and Ti^{4+}): Optical and strong intrinsic room temperature ferromagnetism of perovskite $BaSnO_3$, *J. Alloys Compd.*, 2022, **925**, 166702.

7 M. A. Wahba, S. M. Yakout, A. M. Youssef, W. Sharmoukh, A. M. E. Sayed and M. S. Khalil, Chelating Agents Assisted Rapid Synthesis of High Purity $BiFeO_3$: Remarkable Optical, Electrical, and Magnetic Characteristics, *J. Supercond. Novel Magn.*, 2022, **35**, 3689–3704.

8 T. R. Tatarchuk, N. D. Paliychuk, M. Bououdina, B. Al-Najar, M. Pacia, W. Macyk and A. Shyichuk, Effect of cobalt on structural, elastic, magnetic and optical properties of zinc ferrite nanoparticles, *J. Alloys Compd.*, 2018, **731**, 1256–1266.

9 S. B. Narang and K. Pubby, Nickel Spinel Ferrites: A review, *J. Magn. Magn. Mater.*, 2021, **519**, 167163.

10 S. Zare, A. A. Ati, S. Dabagh, R. M. Rosnan and Z. Othaman, Synthesis, structural and magnetic behavior of Zn–Al substituted cobalt ferrite nanoparticles, *J. Mol. Struct.*, 2015, **1089**, 25–31.

11 G. S. Kumar, T. Raguram and K. S. Rajni, Synthesis and Characterization of Nickel-Substituted Cobalt Ferrite Nanoparticles Using Sol–Gel Auto-combustion Method, *J. Supercond. Novel Magn.*, 2019, **32**, 1715–1723.

12 S. I. Ahmad, Nano cobalt ferrites: Doping, Structural, Low-temperature, and room temperature magnetic and dielectric properties – A comprehensive review, *J. Magn. Magn. Mater.*, 2022, **562**, 169840.

13 L. Ajroudi, N. Mliki, L. Bessais, V. Madigou, S. Villain and C. Leroux, Magnetic, electric and thermal properties of cobalt ferrite nanoparticles, *Mater. Res. Bull.*, 2014, **59**, 49–58.

14 P. Thakur, N. Gahlawat, P. Punia, S. Kharbanda, B. Ravelo and A. Tahkur, Cobalt Nanoferrites: a Review on Synthesis, Characterization, and Applications, *J. Supercond. Novel Magn.*, 2022, **35**, 2639–2669.

15 S. Jauhar, J. Kaur, A. Goyal and S. Singhal, Tuning the properties of cobalt ferrite: a road towards diverse applications, *RSC Adv.*, 2016, **6**, 97694–97719.

16 K. V. Chandekar and K. M. Kant, Strain induced magnetic anisotropy and 3d7 ions effect in $CoFe_2O_4$ nanoplatelets, *Superlattices Microstruct.*, 2017, **111**, 610–627.

17 S. Rasheed, R. A. Khan, F. Shah, B. Ismail, J. Nisar, S. M. Shah, A. Rahim and A. R. Khan, Enhancement of electrical and magnetic properties of cobalt ferrite nanoparticles by co-substitution of Li–Cd ions, *J. Magn. Magn. Mater.*, 2019, **471**, 236–241.

18 K. V. Chandekar and K. M. Kant, Estimation of the spin–spin relaxation time of surfactant coated $CoFe_2O_4$ nanoparticles by electron paramagnetic resonance spectroscopy, *Phys. E*, 2018, **104**, 192–205.

19 A. Milutinović, Z. Ž. Lazarević, M. Šuljagić and L. Andjelković, Synthesis-Dependent Structural and Magnetic Properties of Monodomain Cobalt Ferrite Nanoparticles, *Metals*, 2024, **14**, 833.

20 S. Fiaz, M. Naeem Ahmed, I. Ul Haq, S. W. Ali Shah and M. Waseem, Green synthesis of cobalt ferrite and Mn doped cobalt ferrite nanoparticles: Anticancer, antidiabetic and antibacterial studies, *J. Trace Elem. Med. Biol.*, 2023, **80**, 127292.

21 B. G. Toksha, S. E. Shrisath, M. L. Mane, S. M. Patange, S. S. Jadhav and K. M. Jadhav, Autocombustion high-temperature synthesis, structural, and magnetic properties of $CoCr_xFe_{2-x}O_4$ ($0 \leq x \leq 1.0$), *J. Phys. Chem. C*, 2011, **115**, 20905–20912.

22 T. Zeeshan, S. Waseem, Z. Ejaz, Z. Kayani and T. E. Kuntsevich, Study of electrical conductance and dielectric properties of vanadium doped cobalt ferrites for high frequency applications, *Inorg. Chem. Commun.*, 2024, **162**, 111687.

23 S. Gaffar, A. Kumar and U. Riaz, Synthesis techniques and advanced applications of spinel ferrites: A short review, *J. Electroceram.*, 2023, **51**, 246–257.

24 M. Albino, E. Fantechi, C. Innocenti, A. L. Ortega, V. Bonanni, G. Campo, F. Pineider, M. Gurioli, P. Arosio, T. Orlando, G. Bertoni, C. de, J. Fernandez, A. Lascialfari and C. Sangregorio, Role of Zn^{2+} Substitution on the Magnetic, Hyperthermic, and Relaxometric Properties of Cobalt Ferrite Nanoparticles, *J. Phys. Chem. C*, 2019, **123**, 6148–6157.

25 F. Sharifianjazi, M. Moradi, N. Parvin, A. Nemati, A. J. Rad, N. Sheysi, A. Abouchenari, A. Mohammadi, S. Karbasi, Z. Ahmadi, A. Esmaeilkhanian, M. Irani, A. Pakseresht, S. Sahmani and M. S. Asl, Magnetic $CoFe_2O_4$ nanoparticles doped with metal ions: A review, *Ceram. Int.*, 2020, **46**, 18391–18412.

26 A. B. Patil and R. N. Panda, Synthesis, characterizations and magnetic properties of nanoscale $CoV_xFe_{2-x}O_4$ ($0.0 \leq x \leq 0.9$) materials synthesized *via* sol–gel autocombustion route, *Mater. Chem. Phys.*, 2023, **307**, 128215.

Open Access Article. Published on 18 November 2024. Downloaded on 5/8/2026 8:39:22 PM. This article is licensed under a Creative Commons Attribution 3.0 Unported Licence.

27 Z. K. Heiba, M. B. Mohamed and S. I. Ahmed, Cation distribution with correlated with magnetic properties of cobalt ferrite nanoparticles defective by vanadium doping, *J. Magn. Magn. Mater.*, 2017, **441**, 409–416.
28 T. Huang, Z. Qiu, Z. Hu and X. Lu, Novel method of preparing hierarchical porous $CoFe_2O_4$ by the citric acid-assisted sol–gel auto-combustion for supercapacitors, *J. Energy Storage*, 2021, **35**, 102286.
29 S. Upadhyay, K. Parekh and B. Pandey, Influence of crystallite size on the magnetic properties of Fe_3O_4 Nanoparticles, *J. Alloys Compd.*, 2016, **678**, 478–485.
30 K. V. Chandekar and K. M. Kant, Size-strain analysis and elastic properties of $CoFe_2O_4$ nanoplatlets by hydrothermal method, *J. Mol. Struct.*, 2018, **1154**, 418–427.
31 H. Irfan, R. K. Mohamed and S. Anand, Microstructural evaluation of $CoAl_2O_4$ nanoparticles by Williamson-Hall and size-strain plot methods, *J. Asian Ceram. Soc.*, 2018, **6**, 54–62.
32 M. M. L. Sonia, S. Anand, V. M. Vinosel, M. A. Janifer, S. Pauline and A. Manikanda, Effect of lattice strain on structure, morphology and magneto-dielectric properties of spinel $NiGd_xFe_{2-x}O_4$ ferrite nano-crystallites synthesized by sol–gel route, *J. Magn. Magn. Mater.*, 2018, **466**, 238–251.
33 G. Channagoudra, J. P. J. Nunez, R. L. Hadimani and V. Dayal, Study of cation distribution in La^{3+} and Eu^{3+} substituted cobalt ferrite and its effect on magnetic properties, *J. Magn. Magn. Mater.*, 2022, **559**, 169550.
34 W. Wenwei, C. Jinchao, W. Xuehang, L. Sen and H. Aigui, $Co_{0.35}Mn_{0.65}Fe_2O_4$ magnetic particles: Preparation and kinetics research of thermal process of the precursor, *Powder Technol.*, 2012, **215–216**, 200–205.
35 P. V. V. Romanholo, T. E. P. Alves, J. Swapnalin, P. Banerjee and A. Franco, Tailoring the magnetic properties of Zn doped nickel, magnesium and cobalt ferrite ceramics, *Mater. Chem. Phys.*, 2022, **284**, 126072.
36 E. Puscasu, L. Sacarescu, L. Popescu-Lipan, V. Nica, M. Grigoras, A. Domocos, N. Lupu and D. Creanga, Study on the effect of some surface phenomena on the properties of citrate capped cobalt doped ferrites, *Appl. Surf. Sci.*, 2019, **483**, 1182–1191.
37 S. A. Al-Zahrani, A. Manikandan, K. Thanrasu, A. Dinesh, K. K. Raja, M. A. Almessiere, Y. Slimani, A. Baykal, S. Bhuminathan, S. Raghavendra Jayesh, J. Ahmed, H. S. Alorfi, M. A. Hussein, I. Khan and A. Khan, Influence of Ce^{3+} on the Structural, Morphological, Magnetic, Photocatalytic and Antibacterial Properties of Spinel $MnFe_2O_4$ Nanocrystallites Prepared by the Combustion Route, *Crystals*, 2022, **12**, 268.
38 G. Sharada, N. P. Kumar, P. Sowjanya and D. Sreenivasu, Low concentration doping effects of holmium on structural and spectroscopic properties of cobalt ferrite, *Mater. Today: Proc.*, 2023, **92**, 440–444.
39 R. S. Yadav, I. Kuřitka, J. Vilcakova, J. Havlica, J. Masilko, L. Kalina, J. Tkacz, J. Švec, V. Enev and M. Hajdúchová, Impact of grain size and structural changes on magnetic, dielectric, electrical, impedance and modulus spectroscopic characteristics of $CoFe_2O_4$ nanoparticles synthesized by honey mediated sol–gel combustion method, *Adv. Nat. Sci.: Nanosci. Nanotechnol.*, 2017, **8**, 045002.
40 P. Chandramohan, M. P. Srinivasan, S. Velmurugan and S. V. Narasimhan, Cation distribution and particle size effect on Raman spectrum of $CoFe_2O_4$, *J. Solid State Chem.*, 2011, **184**, 89–96.
41 V. D'Ippolito, G. B. Andreozzi, D. Bersani and P. P. Lottici, Raman fingerprint of chromate, aluminate and ferrite spinels, *J. Raman Spectrosc.*, 2015, **46**, 1255–1264.
42 L. E. Caldeira, C. S. Erhardt, F. R. Mariosi, J. Venturini, R. Y. S. Zampiva, O. R. K. Montedo, S. Arcaro, C. P. Bergmann and S. R. Bragança, Correlation of synthesis parameters to the structural and magnetic properties of spinel cobalt ferrites ($CoFe_2O_4$) – an experimental and statistical study, *J. Magn. Magn. Mater.*, 2022, **550**, 169128.
43 N. Liu, P. Du, P. Zhou, R. G. Tanguturi, Y. Qi, T. Zhang and C. Zhuang, Annealing temperature effects on the cation distribution in $CoFe_2O_4$ nanofibers, *Appl. Surf. Sci.*, 2020, **532**, 147440.
44 P. N. Anantharamaiah and P. A. Joy, Effect of co-substitution of Co^{2+} and V^{5+} for Fe^{3+} on the magnetic properties of $CoFe_2O_4$, *Phys. B*, 2019, **554**, 107–113.
45 C. N. Chervin, J. S. Ko, B. W. Miller, L. Dudek, A. N. Mansour, M. D. Donakowski, T. Brintlinger, P. Gogotsi, S. Chattopadhyay, T. Shibata, J. F. Parker, B. P. Hahn, D. R. Rolison and J. W. Long, Defective by design: vanadium-substituted iron oxide nanoarchitectures as cation-insertion hosts for electrochemical charge storage, *J. Mater. Chem. A*, 2015, **3**, 12059–12068.
46 G. F. Dionne, A Review of Ferrites for Microwave Applications, *Proc. IEEE*, 1975, **63**, 777–789.
47 H. Ghorbani, M. Eshraghi and A. A. S. Dodaran, Structural and magnetic properties of cobalt ferrite nanoparticles doped with cadmium, *Phys. B*, 2022, **634**, 413816.
48 S. B. Dalavi, P. P. Mishra, T. Cherian, M. M. Raja and R. N. Panda, Magnetic and Mössbauer Studies on Nanostructured $CoCr_xFe_{2-x}O_4$ ($0 \leq x \leq 1$) Spinel Ferrites Prepared by Sol–Gel Auto Combustion Method, *J. Nanosci. Nanotechnol.*, 2020, **20**, 983–990.
49 K. Bouferrache, Z. Charifi, H. Baaziz, G. Uğur, Ş. Uğur, B. Boyacıoğlu and H. Ünver, Cation distribution effect on electronic, magnetic structure and optic properties in cobalt ferrites $(Co_{1-y}Fe_y)_{Tet}(Co_yFe_{2-y})_{Oct}O_4$ with disordered spinel structure, *Phys. Scr.*, 2020, **95**, 105801.
50 M. George, S. S. Nair, K. A. Malini, P. A. Joy and M. R. Anantharaman, Finite size effects on the electrical properties of sol–gel synthesized $CoFe_2O_4$ powders: deviation from Maxwell–Wagner theory and evidence of surface polarization effects, *J. Phys. D: Appl. Phys.*, 2007, **40**, 1593–1602.
51 P. Imanipour, S. Hasani, A. Seifoddini, A. Farnia, F. Karimabadi, K. Jahanbani-Ardakani and F. Davar, The possibility of vanadium substitution on Co lattice sites in $CoFe_2O_4$ synthesized by sol–gel autocombustion method, *J. Sol-Gel Sci. Technol.*, 2020, **95**, 157–167.
52 R. S. Yadav, J. Havlica, J. Masilko, L. Kalina, J. Wasserbauer, M. Hajdúchová, V. Enev, I. Kuřitka and Z. Kožáková, Impact

 This journal is © The Royal Society of Chemistry and the Centre National de la Recherche Scientifique 2025

Open Access Article. Published on 18 November 2024. Downloaded on 5/8/2026 8:39:22 PM.
This article is licensed under a Creative Commons Attribution 3.0 Unported Licence.

of Nd^{3+} in $CoFe_2O_4$ spinel ferrite nanoparticles on cation distribution, structural and magnetic properties, *J. Magn. Magn. Mater.*, 2016, **399**, 109–117.

53 Y. Yafet and C. Kittel, Antiferromagnetic Arrangements in Ferrites, *Phys. Rev.*, 1952, **87**, 290–294.

54 V. Vaithyanathan, K. Ugendar, J. A. Chelvane, K. K. Bharathi and S. S. R. Inbanathan, Structural and magnetic properties of Sn and Ti doped Co ferrite, *J. Magn. Magn. Mater.*, 2015, **382**, 88–92.

55 D. M. Ghone, V. L. Mathe, K. K. Patankar and S. D. Kaushik, Microstructure, lattice strain, magnetic and magnetostriction properties of holmium substituted cobalt ferrites obtained by co-precipitation method, *J. Alloys Compd.*, 2018, **739**, 52–61.

56 R. S. Ningthoujam, R. N. Panda and N. S. Gajbhiye, Variation of intrinsic magnetic parameters of single domain Co–N interstitial nitrides synthesized *via* hexa-ammine cobalt nitrate route, *Mater. Chem. Phys.*, 2012, **134**, 377–381.

57 X. Wu, J. Xu, X. Huo, J. Chen, Q. Zhang, F. Huang, Y. Lia, H. Su and L. Li, Nb_2O_5-doped NiZnCo ferrite ceramics with ultra-high magnetic quality factor and low coercivity for high-frequency electronic devices, *J. Eur. Ceram. Soc.*, 2021, **41**, 5193–5200.

58 T. Zhou, H. Zhang, C. Liu, L. Jin, F. Xu, Y. Liao, N. Jia, Y. Wang, G. Gan, H. Su and L. Jia, Li_2O–B_2O_3–SiO_2–CaO–Al_2O_3 and Bi_2O_3 co-doped gyromagnetic $Li_{0.43}Zn_{0.27}Ti_{0.13}Fe_{2.17}O_4$ ferrite ceramics for LTCC Technology, *Ceram. Int.*, 2016, **42**, 16198–16204.

59 K. V. Chandekar and K. M. Kant, Relaxation phenomenon and relaxivity of cetrimonium bromide (CTAB) coated $CoFe_2O_4$ nanoplatelets, *Phys. B*, 2018, **545**, 536–548.

60 K. V. Chandekar and S. P. Yadav, Comprehensive study of MFe_2O_4 (M = Co, Ni, Zn) nanostructures prepared by co-precipitation route, *J. Alloys Compd.*, 2023, **960**, 170838.

61 F. Bødker, S. Mørup and S. Linderoth, Surface effects in metallic iron nanoparticles, *Phys. Rev. Lett.*, 1994, **72**, 282–285.

62 A. B. Patil and R. N. Panda, Magnetic Properties of CoNb$_y$Fe$_{2-y}$O$_4$ ($0.00 \leq y \leq 0.08$) Nanomaterials Synthesized *via* Modified Sol–gel Autocombustion Route, *J. Supercond. Novel Magn.*, 2024, **37**, 597–608.

63 D. Tomar and P. Jeevanandam, Synthesis of cobalt ferrite nanoparticles with different morphologies *via* thermal decomposition approach and studies on their magnetic properties, *J. Alloys Compd.*, 2020, **843**, 15515.

64 K. V. Chandekar and K. M. Kant, Effect of size and shape dependent anisotropy on superparamagnetic property of $CoFe_2O_4$ nanoparticles and nanoplatelets, *Phys. B*, 2017, **520**, 152–163.

65 H. Ghorbani, M. Eshraghi, A. A. S. Dodaran, P. Kameli, S. Protasowicki, C. Johnson and D. Vashaee, Effect of Yb doping on the structural and magnetic properties of cobalt ferrite nanoparticles, *Mater. Res. Bull.*, 2022, **147**, 111642.